An efficient and adaptive approach for modeling gravity effects in spherical coordinates

Zhiwei Li *, Tianyao Hao, Ya Xu, Yi Xu

Key Laboratory of Petroleum Resources Research, Institute of Geology and Geophysics, Chinese Academy of Sciences, Beijing, 100029, China

ARTICLE INFO

ABSTRACT

The need to obtain more reliable Earth structures has been the impetus for conducting joint inversions of disparate geophysical datasets. For seismic arrival time tomography, joint inversion of arrival time and gravity data has become an important way to investigate velocity structure of the crust and upper mantle. However, the absence of an efficient approach for modeling gravity effects in spherical coordinates limits the joint tomographic analysis to only local scales. In order to extend the joint tomographic inversion into spherical coordinates, and enable it to be feasible for regional studies, we develop an efficient and adaptive approach for modeling gravity effects in spherical coordinates based on the longitudinal/latitudinal grid spacing. The complete gravity effects of spherical prisms, including gravitational potential, gravity vector and tensor gradients, are calculated by numerical integration of the Gauss–Legendre quadrature (GLQ). To ensure the efficiency of the gravity modeling, spherical prisms are recursively subdivided into smaller units according to their distances to the observation point. This approach is compatible with the parameterization of regional arrival time tomography for large areas, in which both the near- and far-field effects of the Earth's curvature cannot be ignored. Therefore, this approach can be implemented into the joint tomographic inversion of arrival time and gravity data conveniently. As practical applications, the complete gravity effects of a single anomalous density body have been calculated, and the gravity anomalies of two tomographic models in the Taiwan region have also been obtained using empirical relationships between P-wave velocity and density.

© 2011 Elsevier B.V. All rights reserved.

1. Introduction

The nonuniqueness inherent to all geophysical inversions limits the geological and geophysical understanding of subsurface structures, whereas joint inversion of disparate geophysical datasets provides a feasible way to obtain reliable models with higher accuracy and resolution (Roecker, et al., 2004; Bosch et al., 2006; Vermeesch et al., 2009). Recently, joint inversions of seismic arrival time and gravity data have been conducted using empirical or measured velocity–density relationship constraints (Birch, 1961; Lees and VanDecar, 1991; Masson et al., 1998; Nielsen and Jacobsen, 2000; Afnimar et al., 2002; Roecker et al., 2004; Vermeesch et al., 2009). Subsurface models derived from joint inversion could fit both seismic arrival time and gravity datasets very well, and gravity anomalies also provide important constraints on the lithospheric structures (e.g., von Frese et al., 1997, 1999; Masson et al., 1998; Chen and Ozalaybey, 1998; Bosch et al., 2006; Hao et al., 2007; Asgharzadeh et al., 2007; Xu et al., 2009). This is especially true in areas with sparse seismic ray path samplings, where the resolutions from only arrival time data are low.

As gravity data not only provide important constraints on subsurface structures, but also play an important role in joint inversion with seismic arrival time data, there is a great need for developing an efficient and accurate approach for modeling theoretical gravity effects of three-dimensional models. For tomographic studies of local scale (e.g. 200 km or smaller in lateral directions), the curvature of the Earth may be neglectable. Hence the Cartesian coordinate system is appropriate for modeling this situation (by applying Earth flattening transforms), and gravity effects can be calculated conveniently by using analytic equations of rectangular parallelepiped (Nielsen and Jacobsen, 2000; Afnimar et al., 2002; Roecker et al., 2004; Vermeesch et al., 2009). Whereas for regional to global studies (e.g. more than 200 km in lateral directions), the curvature of the Earth needs to be accounted for in some manner. Earth flattening transforms offer one way of doing this, but as they are specifically applied to great circle paths, they are not convenient for the fixed grid system used in the tomographic method (Li et al., 2009a). As tomographic models are usually built on a mesh of grid points that are regularly spaced in geographic latitude, longitude, and depth, modeling gravity effects in spherical coordinates is a straightforward way for the joint inversion of arrival time and gravity data. An identical coordinate system for arrival time tomography and gravity modeling makes it easy to carry out the joint inversion.

* Corresponding author. Tel.: +86 10 82998104.
  E-mail address: zwli@mail.iggcas.ac.cn (Z. Li).

Due to the complicated integral equations associated with gravity modeling of spherical prisms, numerical approaches are often utilized. The equivalent point source model is introduced to evaluate the gravity effects (e.g. potential, vector and tensor gradient fields) of arbitrary, spherical coordinate distributions of anomalous mass with least-squares accuracy (von Frese et al., 1981a, 1981b; Asgharzadeh et al., 2007). In order to model satellite gravity effects, Asgharzadeh et al. (2007) explicitly developed the elegant Gauss–Legendre quadrature (GLQ) formulae for spherical prisms. An accurate solution could be obtained as long as the node spacing is smaller than the distance between the source and the observation point (Ku, 1977; von Frese et al., 1981b; Asgharzadeh et al., 2007). Considering that the satellite orbit for gravity measurement is at several hundred kilometer altitudes, the distance between the source and the observation point is so large that the highest practical accuracy of numerical integration can often be obtained with a small number of GLQ nodes (Asgharzadeh et al., 2007). However, for joint inversion of arrival time and gravity data, Bouguer gravity anomalies used in the inversion represent the gravity effects of subsurface structures at the sea level. Hence, smaller node spacing must be adopted to ensure the accuracy of the GLQ solution. Utilizing such a small size uniform node spacing for GLQ integration adopted by Asgharzadeh et al. (2007) can become too time consuming to be tractable. From a practical point of view, uniform node spacing for all prisms through the whole model is unnecessary, node spacing for each prism should be determined according to the distance between each prism and the observation point. Moreover, if the size of the prism is comparable with the distance between the prism and the observation point, node spacing for different parts of the prism should also be adjustable to prevent redundant computation. Therefore, an adaptive strategy should be considered on gravity modeling to ensure the efficiency and accuracy simultaneously.

The motivation of this study is to develop an efficient and adaptive approach for modeling gravity effects at sea level in spherical coordinates, which should be capable of dealing with large computations associated with regional models in joint inversions of arrival time and gravity data. In the following sections, the adaptive scheme for subdividing prisms has been conducted to obtain an accurate solution, and the performance of this approach has also been well tested by comparisons with a previous approach, in which uniform node spacing for GLQ integration is adopted. As applications, the gravity potential, vector and tensor gradient fields of a single anomalous body have been modeled, and gravity anomalies of two three-dimensional velocity models in the Taiwan region have been also calculated.

2. Method

2.1. Gravity effects for spherical prism

Based on the potential field theory, the gravity effects (i.e. gravitational potential, spatial vector and tensor gradients of the scalar gravitational potential) for one spherical prism at observation point o can be expressed as a triple integral (Asgharzadeh et al., 2007):

$$g_o = \int_{r_s=r_1}^{r_2} \int_{\theta_s=\theta_1}^{\theta_2} \int_{\phi_s=\phi_1}^{\phi_2} g(r_s,\theta_s,\phi_s,r_o,\theta_o,\phi_o)\,dr_s d\theta_s d\phi_s \qquad (1)$$

where g_o represents the different gravity effects at the observation point o, $g(r_s,\theta_s,\phi_s,r_o,\theta_o,\phi_o)$ represents the integral kernel of the corresponding gravity effect (Table 1 in details); r_s, θ_s, ϕ_s and r_o, θ_o, ϕ_o are the radius, geocentric colatitude, and longitude coordinates of the source and observation points; r_1, θ_1, ϕ_1 and r_2, θ_2, ϕ_2 are the corner coordinates of the radius, geocentric colatitude, and longitude of the

Table 1
Formulae for integral kernels of all gravity effects (Asgharzadeh et al., 2007).

Parameter[*]	$g(r_s,\theta_s,\phi_s,r_o,\theta_o,\phi_o)$
k	$G\rho_s r_s^2 \sin\theta_s$
P	k/R_{os}
g_r	$k(-r_o + r_s\cos\delta)/R_{os}^3$
g_θ	$kr_s[-\sin\theta_o\cos\theta_s + \cos\theta_o\sin\theta_s\cos(\phi_o-\phi_s)]/R_{os}^3$
g_ϕ	$-kr_s\sin\theta_s\sin(\phi_o-\phi_s))/R_{os}^3$
g_{rr}	$k(-R_{os}^2 + 3(r_o - r_s\cos\delta)^2)/R_{os}^5$
$g_{r\theta}$	$kr_s[-\sin\theta_o\cos\theta_s + \cos\theta_o\sin\theta_s\cos(\phi_o-\phi_s)][R_{os}^2 + 3r_o(-r_o + r_s\cos\delta)]/R_{os}^5$
$g_{r\phi}$	$kr_s\sin\theta_o\sin\theta_s\sin(\phi_o-\phi_s)[-R_{os}^2 + 3r_o(r_o - r_s\cos\delta)]/R_{os}^5$
$g_{\theta r}$	$3kr_s(r_o - r_s\cos\delta)[\sin\theta_o\cos\theta_s - \cos\theta_o\sin\theta_s\cos(\phi_o-\phi_s)]/R_{os}^5$
$g_{\theta\theta}$	$kr_s(-R_{os}^2\cos\delta + 3r_o r_s[\sin\theta_o\cos\theta_s - \cos\theta_o\sin\theta_s\cos(\phi_o-\phi_s)]^2)/R_{os}^5$
$g_{\theta\phi}$	$kr_s\sin\theta_s\sin(\phi_o-\phi_s)\{-R_{os}^2\cos\theta_o + 3r_o r_s\sin\theta_o[\sin\theta_o\cos\theta_s - \cos\theta_o\sin\theta_s\cos(\phi_o-\phi_s)]\}/R_{os}^5$
$g_{\phi r}$	$3kr_s\sin\theta_s\sin(\phi_o-\phi_s)(r_o - r_s\cos\delta)/R_{os}^5$
$g_{\phi\theta}$	$3kr_o r_s^2\sin\theta_s\sin(\phi_o-\phi_s)[\sin\theta_o\cos\theta_s - \cos\theta_o\sin\theta_s\cos(\phi_o-\phi_s)]/R_{os}^5$
$g_{\phi\phi}$	$kr_s\sin\theta_s[-R_{os}^2\cos(\phi_o-\phi_s + 3r_o r_s\sin\theta_o\sin\theta_s\sin^2(\phi_o-\phi_s)]/R_{os}^5$

[*] Where G is the gravitational constant [$6.67 \times 10^{-11}\,\mathrm{m^3\,kg^{-1}\,s^{-2}}$], and ρ_s is the residual density of spherical prism. P is the gravitational potential, g_r, g_θ, and g_ϕ, are radial, north–south, and east–west gravity vector components; g_{rr}, $g_{r\theta}$, $g_{r\phi}$, $g_{\theta r}$, $g_{\theta\theta}$, $g_{\theta\phi}$, $g_{\phi r}$, $g_{\phi\theta}$, and $g_{\phi\phi}$, are gravity tensor gradient components.

prism. R_{os} represents the distance from a node in the source prism to the observation point, which is given by

$$R_{os} = \left(r_o^2 + r_s^2 - 2r_o r_s \cos\delta\right)^{1/2} \qquad (2)$$

where

$$\cos\delta = \cos\theta_o\cos\theta_s + \sin\theta_o\sin\theta_s\cos(\phi_o-\phi_s). \qquad (3)$$

By substituting Eqs. (2)–(3) into the formulae of all gravity effects (Table 1) and substituting the corresponding $g(r_s,\theta_s,\phi_s,r_o,\theta_o,\phi_o)$ into Eq. (1), the integration formulae for modeling all gravity effects are obtained. For a direct comparison with previous studies, the Observation-centered convention has been adopted to determine the signs of gravity effects (Asgharzadeh et al., 2007).

2.2. Gauss–Legendre quadrature integration

Due to the complicated nature of analytical integration in Eq. (1), the numerical integration of GLQ has been adopted to evaluate the triple integral of Eq. (1) with a least-squares numerical solution (Stroud and Secrest, 1966; von Frese, et al., 1981b; Asgharzadeh et al., 2007). Following the GLQ decomposition, the integral Eq. (1) can be rewritten as below:

$$\frac{(r_2-r_1)(\theta_2-\theta_1)(\phi_2-\phi_1)}{8} \sum_{k=1}^{K}\sum_{j=1}^{J}\sum_{i=1}^{I} C_i C_j C_k\, g\left(r_{si},\theta_{sj},\phi_{sk},r_o,\theta_o,\phi_o\right) \qquad (4)$$

where the number of nodes (I, J, K) are for GLQ integration of r, θ, ϕ coordinates, then the gravity effects of $I \times J \times K$ equivalent point sources are summed to simulate the effects of the spherical prism. The coordinates $(r_{si}, \theta_{sj}, \phi_{sk})$ are the actual coordinates within the prism, and the Gauss–Legendre coefficients (C_i, C_j, C_k) correspond to the coordinates $(r_{ip}, \theta_{jp}, \phi_{kp})$ of the Gaussian node in the interval $(-1, 1)$. r_{si}, θ_{sj}, ϕ_{sk} are given by:

$$\begin{cases} r_{si} = \dfrac{r_{ip}(r_2-r_1) + (r_2 + r_1)}{2} \\[2mm] \theta_{sj} = \dfrac{\theta_{jp}(\theta_2-\theta_1) + (\theta_2 + \theta_1)}{2} \\[2mm] \phi_{sk} = \dfrac{\phi_{kp}(\phi_2-\phi_1) + (\phi_2 + \phi_1)}{2}. \end{cases} \qquad (5)$$
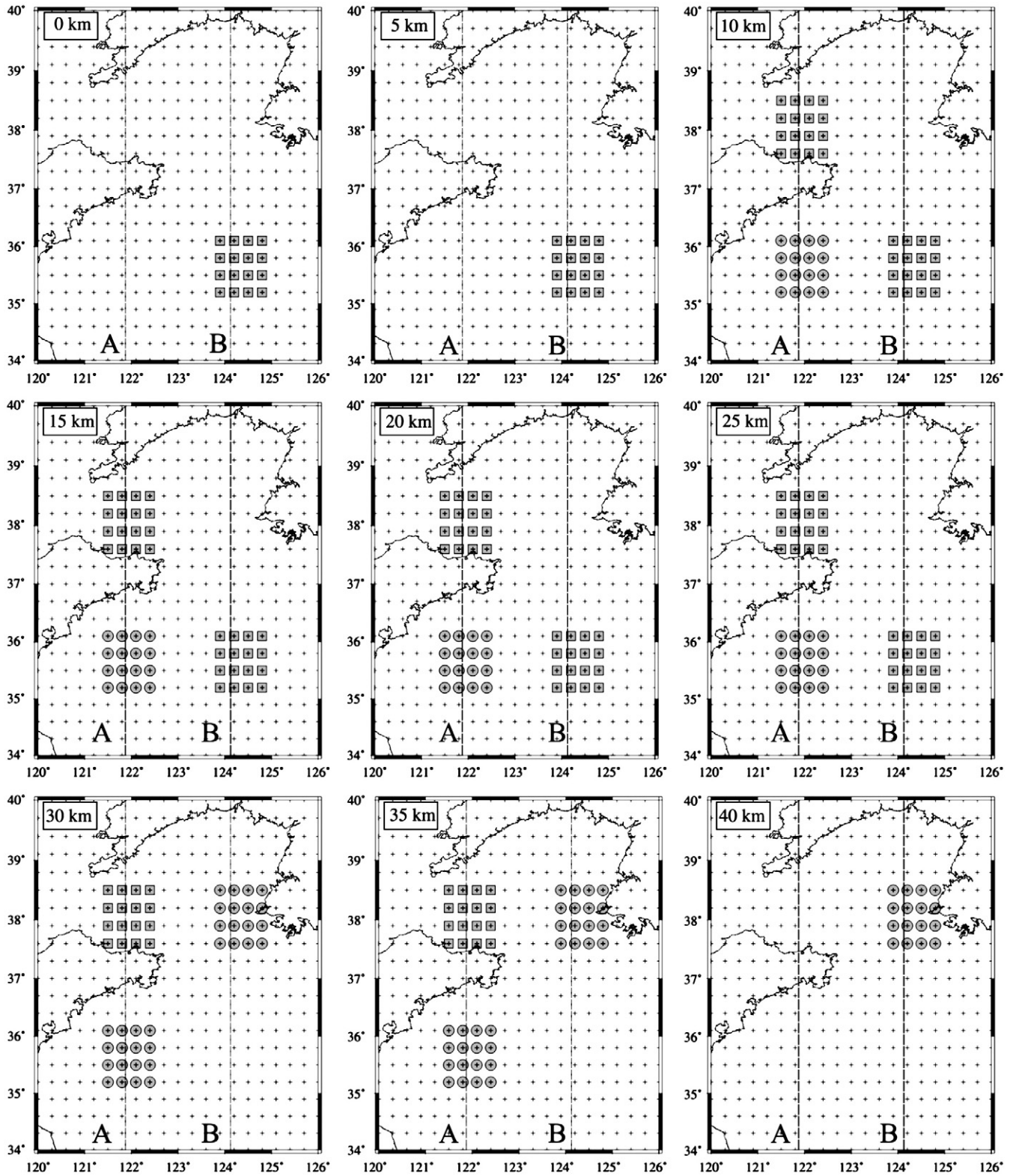
Fig. 1. Synthetic density model in spherical coordinates. Gray squares indicate the grid points with 10% density residuals, and gray circles are the grids with −10% density residuals. Dashed lines represent two profiles for gravity analysis. Grid point locations are indicated by small crosses.

Since r_{si} is always less than r_2 according to Eq. (5), then R_{os} is always greater than zero. Therefore, the GLQ technique to the gravity modeling of ground measurements (i.e., the observation point is atop the spherical prism) will not cause singularities.

2.3. Adaptive scheme of GLQ integration for spherical prism

The accuracy of GLQ integration generally depends on the node spacing, the smaller the node spacing, the more accurate solutions will

Table 2

Synthetic density model for numerical experiments. The anomalous densities for calculating gravity effects are ±10% relative to the 1-D background model.

Depth (km)	Density (g/cm³)	Positive residuals (g/cm³)	Negative residuals (g/cm³)
0	2.60	0.260	−0.260
5	2.72	0.272	−0.272
10	2.72	0.272	−0.272
15	2.72	0.272	−0.272
20	2.72	0.272	−0.272
25	2.92	0.292	−0.292
30	2.92	0.292	−0.292
35	2.92	0.292	−0.292
40	3.32	0.332	−0.332

be. Moreover, numerical accuracy obtained with smaller prisms is equivalent to that obtained with small node spacing for GLQ integration. In order to ensure sufficient accuracy for the gravity modeling, we prefer to subdivide each prism into smaller units rather than decrease the node spacing. Before the GLQ integration, the prism

will be subdivided into smaller units if the maximum side lengths of the prism are greater than the minimum distance between the source prism and the observation points to a certain extent. Subdividing will continually be applied on the smaller prisms recursively until all prisms are small enough compared to the distance between the source and the observation point (for the details, see Appendix A). The advantages of this approach include (1) subdividing for each prism will not introduce any approximations into the gravity modeling; (2) the subdividing is much more efficient than the GLQ integration of equivalent node spacing; (3) node spacing for GLQ integration could also be determined conveniently for a different part of the prism after subdividing, which means the node spacing becomes sparser with the increasing distance between the source and the observation point. Therefore, a more efficient performance than the uniform node spacing for GLQ integration will be achieved. After the source region has been subdivided optimally, the GLQ integration will next be implemented to calculate the gravity effects. In practice, the lower limit of the minimum side length of the prism is set to prevent the program from infinitely or excessively subdividing when the distance to the observation point is zero or close to zero (e.g. the observation point is
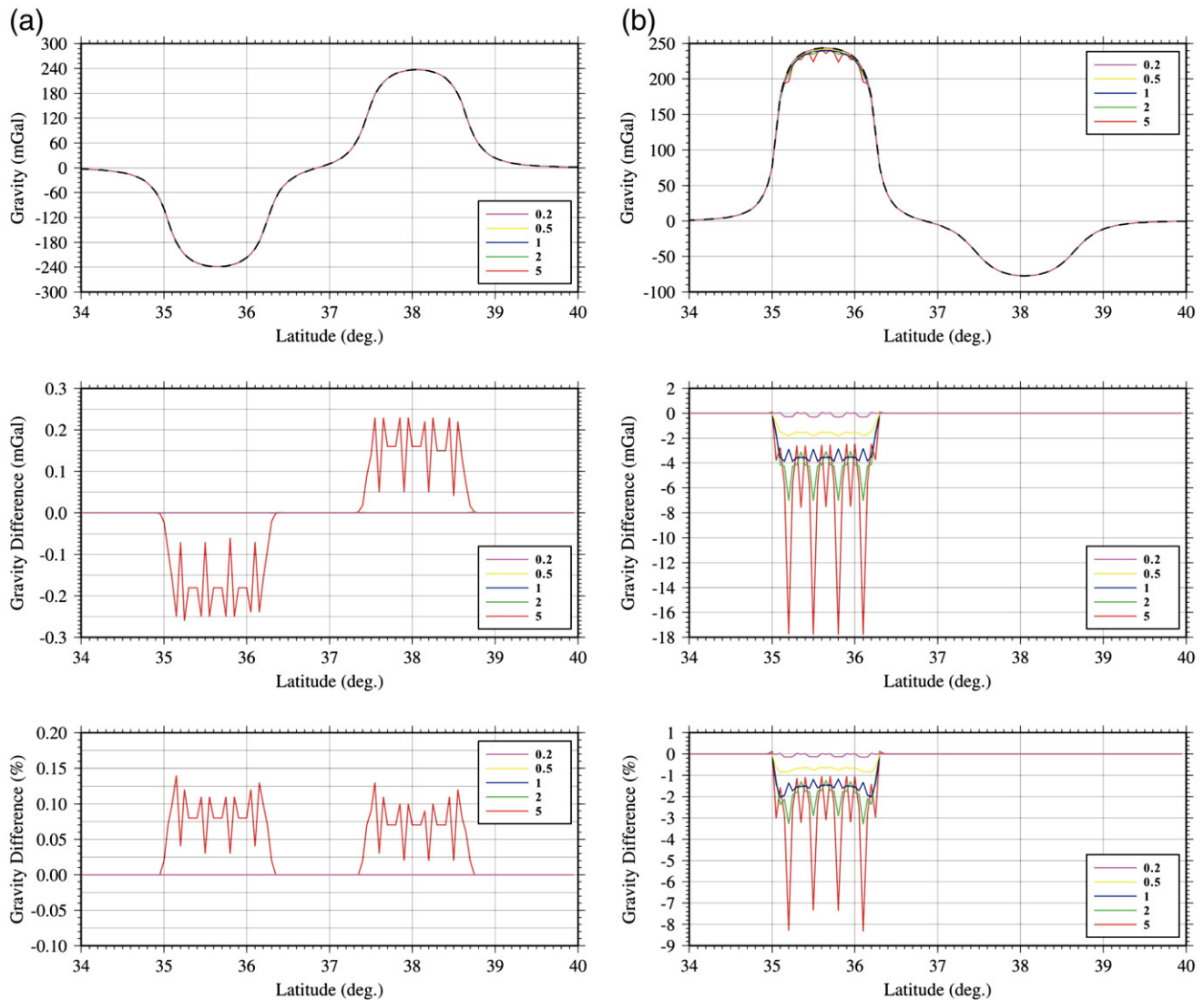

Fig. 2. Gravity anomalies along profiles A (figure a) and B (figure b) from GLQ integration with a different node spacing uniformly distributed for all prisms in the synthetic model. Node spacing of GLQ is 5, 2, 1, 0.5, 0.2, and 0.1 km, and the corresponding gravity anomalies are shown by lines with different colors. Upper maps are the gravity anomalies, where the dashed black line represents the gravity with 0.1 km node spacing; middle ones are the differences between solutions with node spacings of 5, 2, 1, 0.5 and 0.2 km and the solutions with 0.1 km node spacing; lower ones are the percentage (%) of the gravity differences as middle ones.
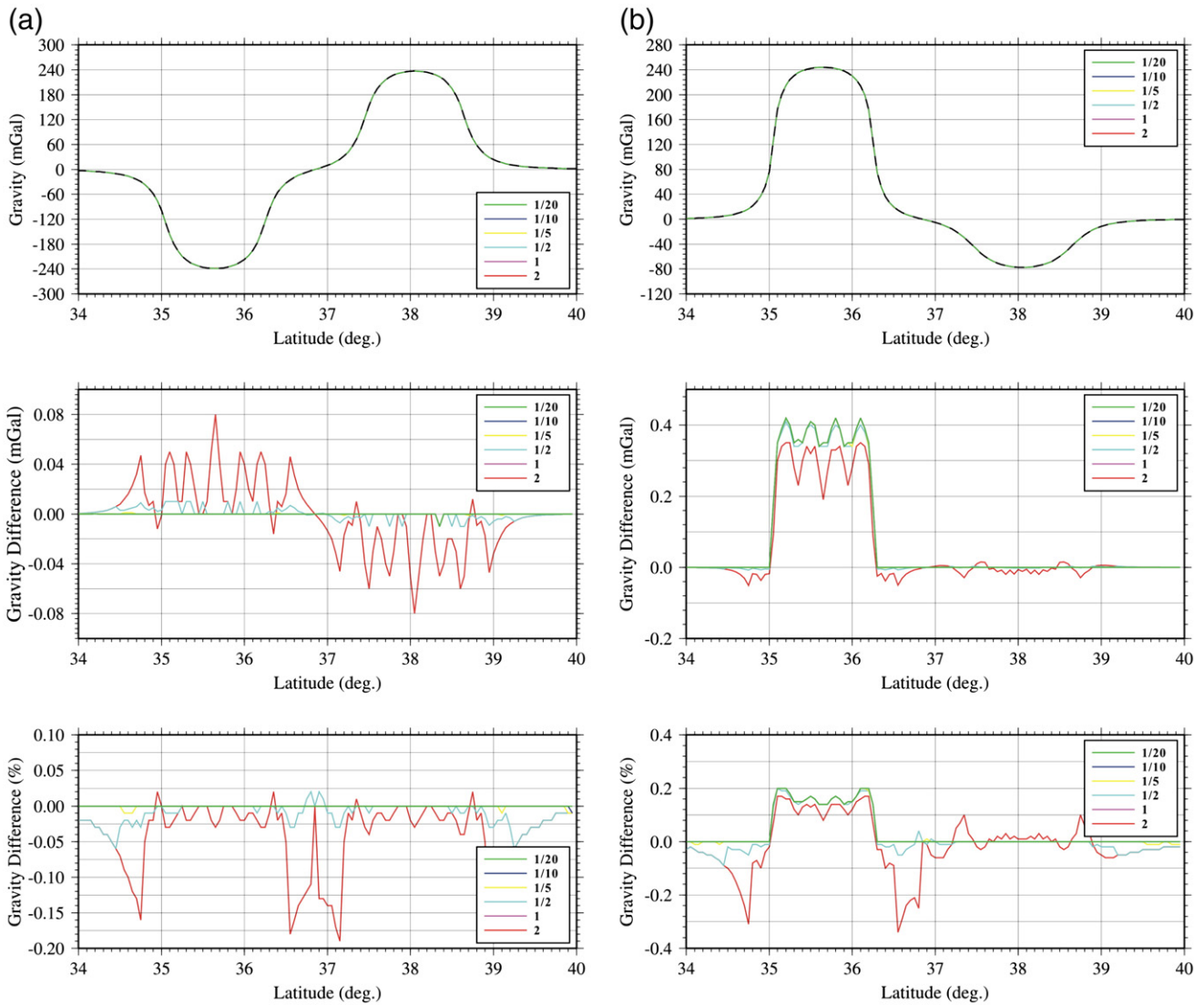
Fig. 3. A similar figure as Fig. 2 except that gravity is calculated by the adaptive approach. *NS* is set to be 1/2, 1, 2, 5, 10 and 20. *MinPrismS* is set to be 0.1 km (for the meaning of *NS* and *MinPrismS*, see Appendix A). Reference gravity anomalies for calculating the differences are taken from the solution with a uniform node spacing of 0.1 km (dashed lines in the upper maps).

atop the prism). If the side length of the prism has already been less than the lower limit of minimum side length, subdividing will be stopped and the GLQ integration will be conducted on this prism.

Although the rapid development of computation technology may reduce the burden of the numerical integration in gravity modeling, an efficient and accurate approach is always needed to conduct many trials in the geophysical inversions to achieve an optimized solution. Smaller prisms and closer spaced node spacing result in a more accurate solution, but at a cost of increased computational time. Previous studies indicate that as long as the node spacing for GLQ integration is less than the distance between the source and the observation point, the accuracy of numerical integration remains essentially unchanged for a different node spacing (Ku, 1977; von Frese et al., 1981b; Asgharzadeh et al., 2007). This conclusion is also valid for the size of the prism. Since the distances between all prisms in the model and the observation point vary from 0 (e.g., atop the surface of the model) to hundreds of kilometers (to the far corner of the model bottom), prism subdivision will gradually reduce with the increase of the distance between the source and the observation point. Most subdivision and computation are conducted on a few prisms close to the observation point, while other prisms far away

from the observation point only require a few computations. Therefore, the adaptive scheme could avoid lots of unnecessary computations on the condition that required accuracy is satisfied.

3. Analysis

3.1. Model parameterization

With the three-dimensional velocity model from tomographic inversion, a density model can be obtained by presuming a functional relationship between density and P-wave velocity based on laboratory measurements (Birch, 1961; Gardner et al., 1974; Christensen and Mooney, 1995; Roecker et al., 2004; Vermeesch et al., 2009). Only the residual density relative to the 1-D model is used to calculate the gravity anomalies. As the density remains constant across the prism in the GLQ integration, the density of each grid in the model is presumed constant within a cube with the grid at the center. Since the density model is constructed in the geographic coordinates with a mesh of grid points regularly spaced in geographic longitude, latitude and depth (Fig. 1), it is compatible with the coordinate system widely used in the regional tomography study. Considering the flattening of the
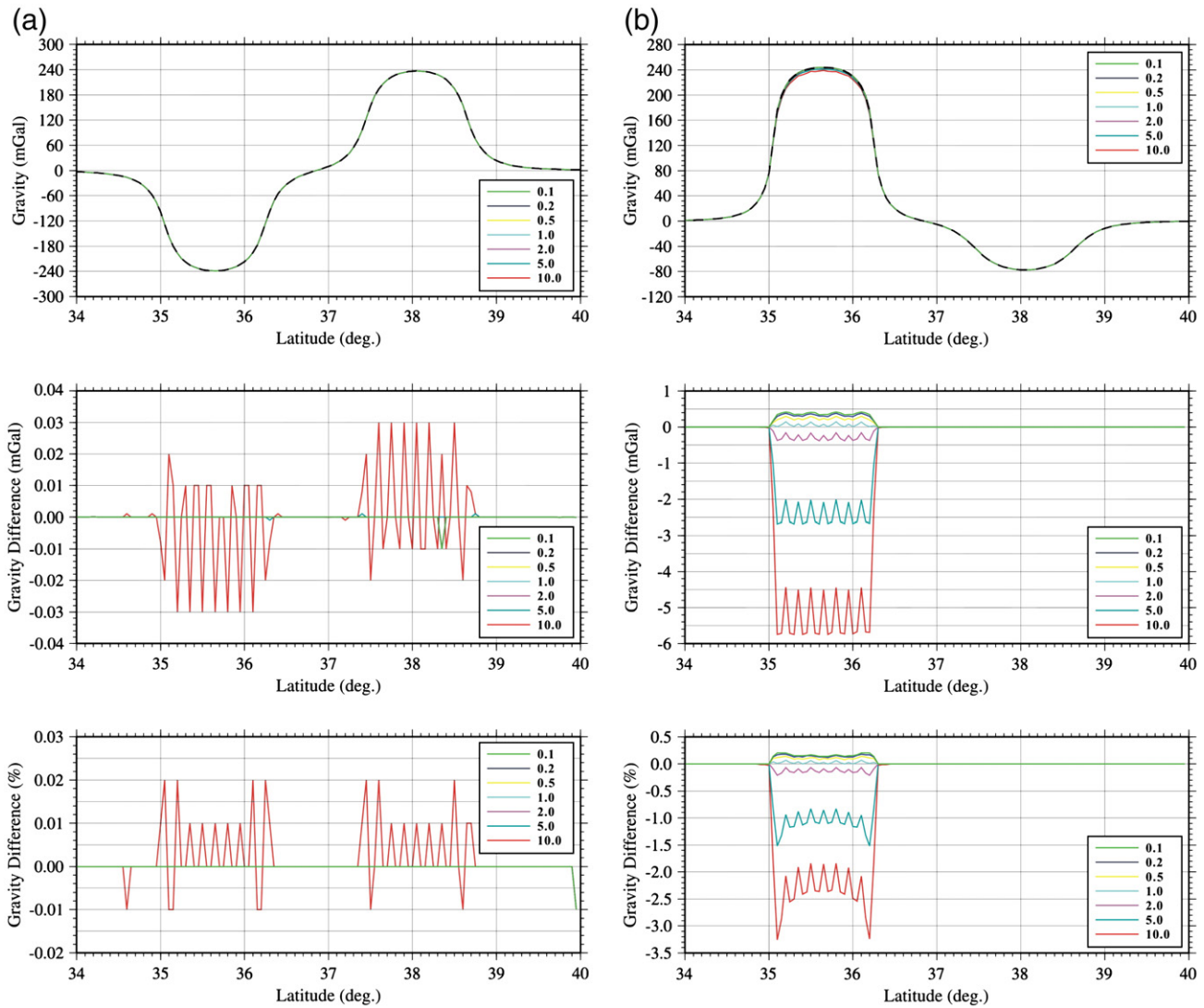
(a)

(b)

Fig. 4. A similar figure as Fig. 3 except that *NS* is 10, and *MinPrismS* is set to be 10, 5, 2, 1, 0.5, 0.2 and 0.1 km.

Earth, the geographic system is transformed into geocentric coordinates as done in regional arrival time tomography.

3.2. Numerical experiments

A synthetic density model is constructed to verify our approach. As shown in Fig. 1, the synthetic model is characterized by simple density anomalies: four 10% positive or negative anomalous bodies are located at different places and depths (relative to the 1-D background model, see Table 2). Observation points along profiles A and B are all at sea level with a lateral interval of 0.05°. Numerical experiments are conducted to evaluate the effects of *NS* and *MinPrismS* on the accuracy of gravity modeling solutions (*NS* is the ratio of the minimum distance between the source prism and the observation point vs the maximum side length of the source prism, and *MinPrismS* is the lower limit of the minimum side length of the source prism). As the 0.1 km uniform node spacing is usually adopted by terrain correction for regional gravity surveys (Smith et al., 2001; Fullea et al., 2008), then the gravity effects with a 0.1 km uniform node spacing for GLQ integration are taken as the references to analyze other solutions with different parameters.

The first experiment shows the gravity effects along profiles A and B (Fig. 1) calculated with different node spacings (5, 2, 1, 0.5,

0.2, and 0.1 km) for GLQ integration uniformly distributed for all prisms in the model. For profile A (Fig. 2a), except that the gravity differences between the solutions with 5 and 0.1 km node spacing reaches its maximum of 0.25 mGal (0.15%), other solutions are essentially the same (lines represented these solutions almost overlap). Whereas for profile B (Fig. 2b), the maximal gravity difference between solutions with 5 km and 0.1 km node spacings reaches 18 mGal (more than 8%). With the decrease of node spacing, the maximal differences also decrease to less than 2 mGal (1%) for the solution of 0.5 km node spacing, and become much smaller for the 0.2 km node spacing.

The second experiment adopts the identical *MinPrismS* (0.1 km) but with different *NS* of 1/2, 1, 2, 5, 10, and 20 (Fig. 3). Gravity solutions with different *NS* on profile A show a very small difference (less than 0.08 mGal or 0.2% when *NS* equals 1/2). For profile B, all differences are less than 0.5 mGal (0.4%), suggesting that the accuracy is not sensitive to *NS* when *MinPrismS* is small (0.1 km) and *NS* equals 1 or larger values.

The third experiment fixes *NS* to be 10 and adjusts *MinPrismS* to be 10, 5, 2, 1, 0.5, 0.2, and 0.1 km (Fig. 4). For profile A, except that the solutions with *MinPrismS* = 10 km have relatively large differences (0.03 mGal or 0.02% maximally), other solutions are essentially the

same (less than 0.01 mGal). For profile B, when *MinPrismS* is less than 5 km, the maximal differences are all less than 0.5 mGal (0.2%).

The fourth experiment provides comparisons between the solutions of uniform node spacing for GLQ integration and the adaptive approach proposed by this study (Fig. 5). The observation point is at (E124.1250, N35.5500) and the elevations vary from 0.1 to 200 km. Different uniform node spacings (10, 5, 2, 1, 0.5, 0.2, and 0.1 km,) are used in the former approach, while different *MinPrismS* (10, 5, 2, 1, 0.5, 0.2, and 0.1 km) and *NS* = 10 are used in the later one. As shown in Fig. 5, when the elevation increases to 1 km, the gravity differences relative to the solution of uniform node spacing of 0.1 km for all *MinPrismS* become less than 0.5 mGal. Whereas for the approach with uniform node spacing, until the elevation increases to 5 km, the gravity differences decrease below 0.5 mGal, suggesting the fast convergence and high accuracy of the adaptive approach.

Above experiments suggest that the accuracy of gravity modeling will be improved with the decrease of the prism's size and the increase of the distance between the prism and the observation point. Relative larger errors appear right upon the density anomalous bodies along

profile B due to the observation point that is atop the prism. However, by choosing proper parameters of *NS* and *MinPrismS*, the accuracy of gravity effects (<0.5%) calculated by our approach can satisfy the needs of regional joint inversion of arrival time and gravity data. The above numerical experiments show that in order to obtain accurate gravity solutions at sea level (e.g. <0.5%), *NS*>1 and *MinPrismS*<1.0 km are reasonable values for our approach. Although only the comparisons of radial gravity are shown in the above experiments, *NS* and *MinPrismS* have similar effects for other gravity effects due to their similar formulae. Since the once, twice, and third power of the distance between the source and the observation point are the denominators in the formulae of gravity potential, vector and tensor gradient field (Table 1), the gravity effects have different sensitivities to the distance. Therefore, a stricter criterion with *NS* = 10 and *MinPrismS* = 0.1 km is adopted in the following experiments to achieve solutions with required accuracy.

Fig. 6 shows the node distributions for GLQ integration with *NS* = 10 and *MinPrismS* = 0.1 km (the observation point is at E124.1250, N35.5500, 0 km). Horizontal and vertical profiles along the depth,
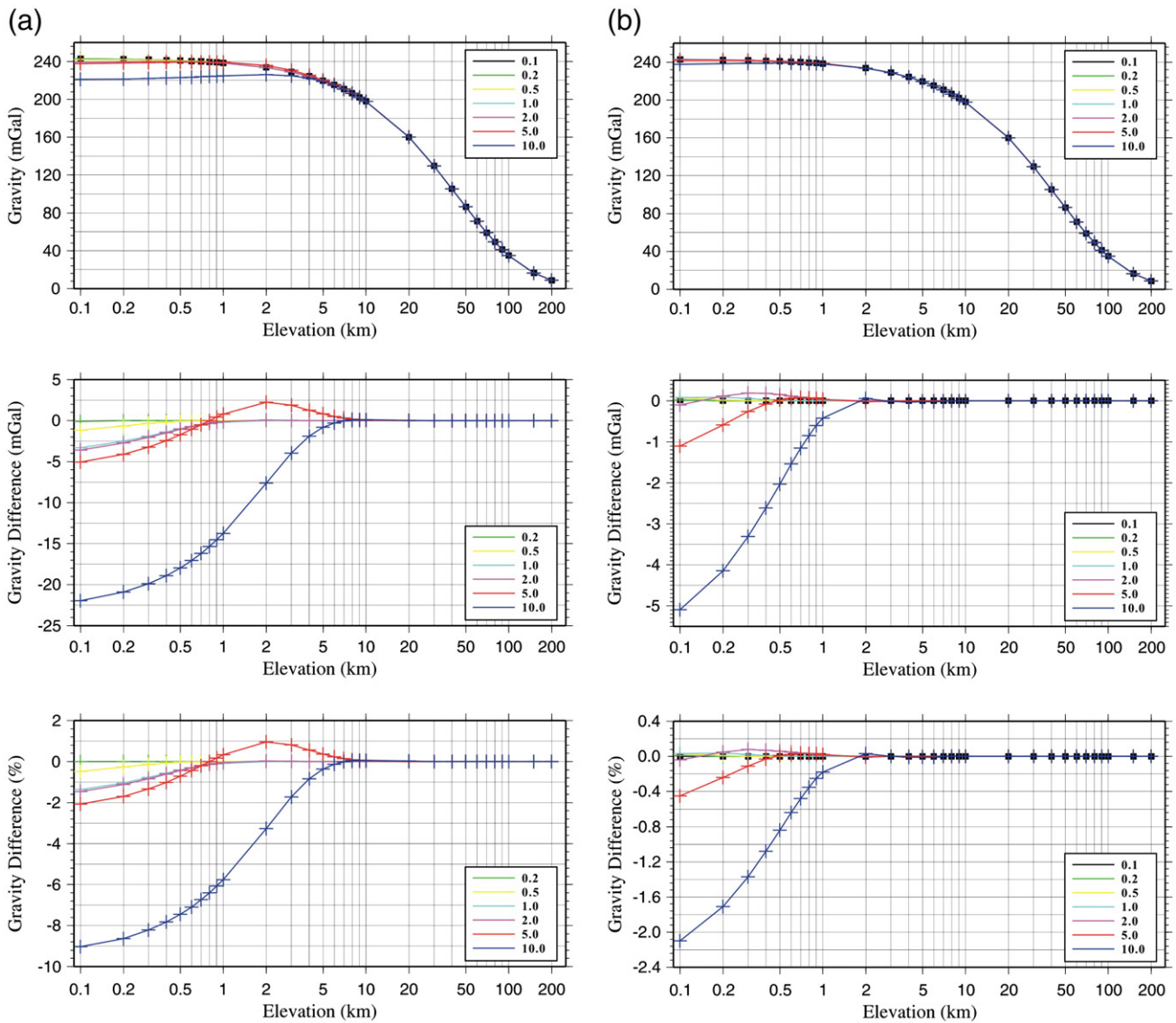

Fig. 5. Gravity anomalies for the observation point (E124.1250, N35.5500) with different elevations from 0.1 to 200 km. (a) Gravity anomalies (upper), gravity differences (middle), and percentages of gravity differences (lower) calculated with uniform node spacing (10, 5, 2, 1, 0.5, 0.2 and 0.1 km) for all prisms. (b) The results calculated by the adaptive approach with *NS* = 10 and *MinPrismS* is set to be 10, 5, 2, 1, 0.5, 0.2 and 0.1 km. Gravity anomalies with uniform node spacing of 0.1 km (black squares in the left panel) are taken as the reference for calculating differences. Crosses indicate the gravity values for all elevations. Black squares in the right panel indicate gravity anomalies with *MinPrismS* equals 0.1 km.

latitude, and longitude all show that the nodes are dense at the area close to the observation point, and gradually become sparse farther away from the observation point. As the number of nodes for GLQ

Fig. 6. Node distributions for GLQ integration beneath the observation point (E124.1250, N35.5500). (a) Horizontal node distribution for prisms at 7.5–12.5 km depth; (b) vertical node distribution of the prisms at latitude of N35.5500; (c) vertical node distribution of the prisms at longitude of E124.1250. Small gray crosses indicate the positions of GLQ nodes. Black crosses are the model grids assigned the density value. Black squares represent the location of the observation point. *NS* is 10, and *MinPrismS* is 0.1 km.

integration has decreased a lot, computations could be saved compared to uniformly distributed GLQ nodes. Within a similar accuracy, our approach is more efficient than the approach with uniform node spacing for GLQ integration. For example, in the fourth experiment (Fig. 5), the computational time is about 1376 s on Xeon CPUs with 0.1 km uniform distributed nodes (only the prisms with anomalous density are involved in the computation, hence the computation will be huge if all prisms in the model are involved). Whereas using the adaptive approach with $NS = 10$ and $MinPrismS = 0.1$ km, the computational time decreases to 3.1 s when the observation point is at 0.1 km elevation, suggesting the highly efficient performance of the adaptive approach.

4. Applications

The gravity effects of potential, vector and tensor gradients are modeled for a $1.2° \times 1.2° \times 27.5$ km prism with a positive density of 10% relative to the 1-D background model (Table 2). The observation points are all at sea level, and the top and bottom of the anomalous body are at 5 and 32.5 km depths. The patterns for all gravity effects (Fig. 7) are similar to the results of Asgharzadeh et al. (2007) at the altitude of 250 km. However, the gravity effects at sea level are much closer to the anomalous bodies and could reflect more details of the substructure.

The gravity anomalies of two three-dimensional velocity models in the Taiwan region are also modeled by our approach. One model is from the individual inversion of P- and S-wave arrival time only (Li et al., 2009b), and another one is the preliminary result from the joint inversion of arrival time and gravity data by the method proposed by Roecker et al. (2004). The spherical finite difference technique is used to implement the 3-D ray tracing (Li et al., 2009a). The P and S arrival times are from the seismic station networks in the Taiwan region during 1992–2004, which consists of about 135,000 P and 77,000 S arrivals from nearly 6000 events at 92 stations (Li et al., 2009b). For the joint inversion, the arrival time and gravity data are involved in the inversion simultaneously. Note that the two models all fit arrival time data very well. Bouguer gravity data used in the joint inversion consist of 603 readings and approximately cover most part of the Taiwan island (Yen et al., 1995). To calculate the gravity anomalies, the P-wave velocity models are converted to density models based on the empirical relationships between P-wave velocity and density (Gardner et al., 1974; Christensen and Mooney, 1995; Roecker et al., 2004).

The primary result of joint inversion is consistent with both types of data, but still remains close to the model consisting of a best fit to the arrival time data. The primary improvement in the 3-D velocity model from joint inversion focuses on the structure near the Moho discontinuity and deeper depth compared to that obtained from the seismic data only, where the seismic ray paths are relatively sparse in this depth, suggesting that gravity data do provide additional information in the velocity model in the Taiwan region. Whereas for the shallower depth in the crust, the main features of the two models remain intact, and hence the interpretations based on the arrival time model remain the same. Synthetic gravity anomalies are calculated from the two tomographic models and compared to the observed Bouguer gravity (Fig. 8). Gravity anomalies from joint inversion are quite similar to the observations. The correlation coefficient reaches 0.70, and the gravity residuals for most observation points are less than 20 mGal. Small scale gravity residuals may relate to the shallow small scale structures, so that the coarse grid spacing of the tomographic model (~10 km laterally and 4–16 km vertically) can't compensate these gravity anomalies (Li et al., 2009b). Compared with synthetic gravity anomalies of the model from arrival time inversion only, the pattern has significant discrepancies and the correlation coefficient is as low as 0.23. Gravity residuals also exceed 40 mGal for most observation points, and the amplitudes of the residuals are comparable with the observation values. It suggests that the model
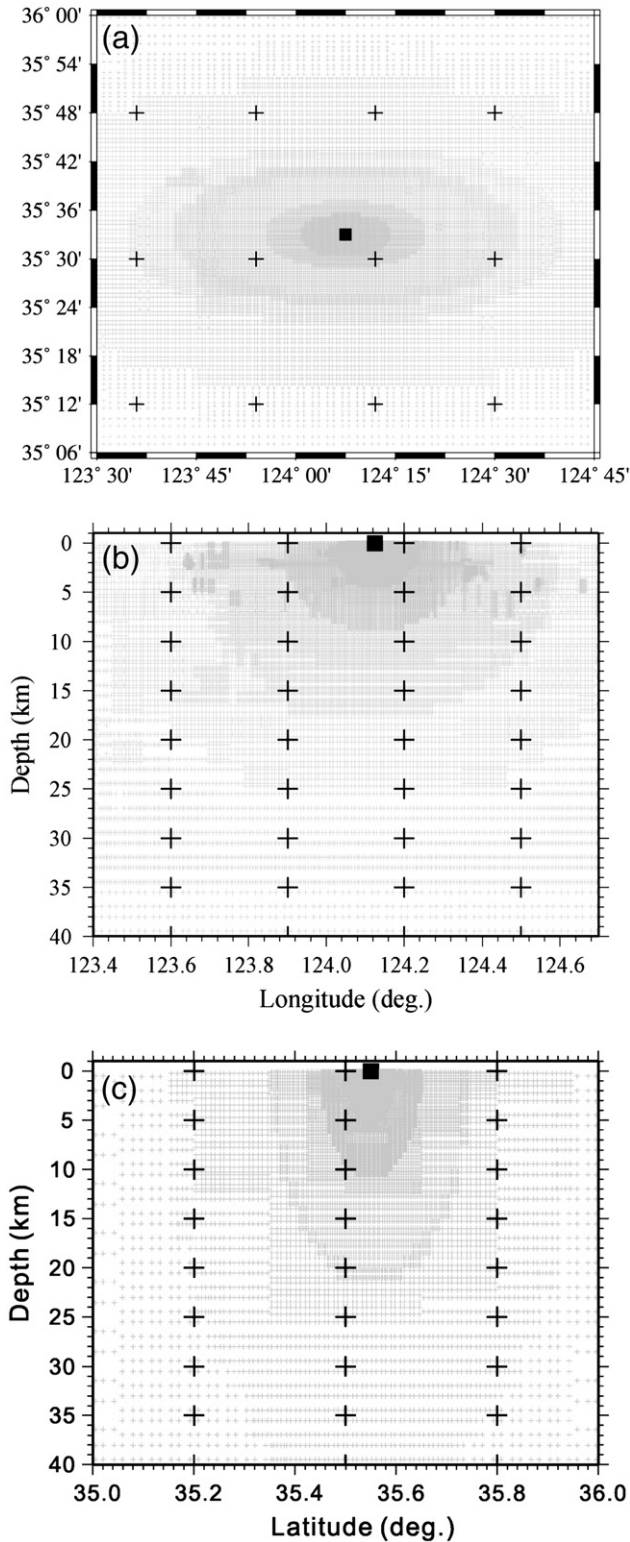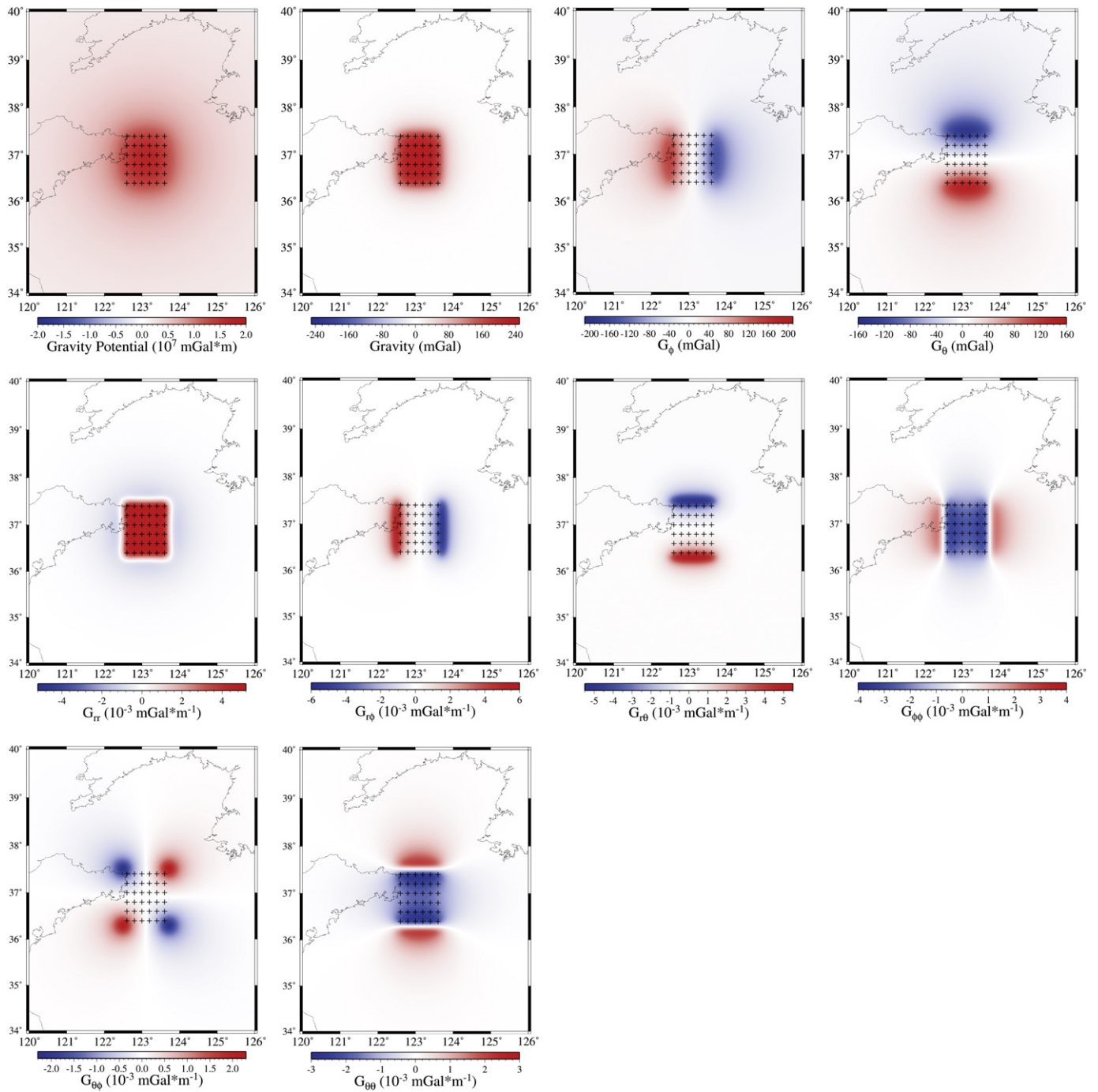
Fig. 7. Gravity effects (i.e. potential, vector and tensor gradient fields) of a single density anomalous body located at 5–32.5 km depth. Grid locations with density anomalies are indicated by small crosses. The three off-diagonal elements of the gravity tensor gradient are symmetric (i.e. $g_{r\theta} = g_{\theta r}$, $g_{r\phi} = g_{\phi r}$, and $g_{\theta\phi} = g_{\phi\theta}$), hence only six unique components of gravity tensor gradient are presented (i.e. g_{rr}, $g_{r\phi}$, $g_{r\theta}$, $g_{\phi\phi}$, $g_{\phi\theta}$, $g_{\theta\theta}$).

from arrival time data only can't fit the gravity data very well, which shows the necessity to conduct the joint inversion of arrival time and gravity data to fit both observations simultaneously.

5. Conclusions

An efficient and adaptive approach for modeling gravity potential, vector and tensor gradient fields is developed in spherical coordinates. This approach adopts the numerical integration of GLQ to prevent the modeling from complicated and daunting analytical integrations. Efficient performance and implementation in spherical

coordinates makes this approach feasible for gravity modeling in the joint inversion of arrival time and gravity data for regional studies. As arrival time tomography has become a routine work for investigating the lithospheric structure, based on the three-dimensional velocity model and relationships between P-wave velocity and density, partial derivative matrix relating observed gravity anomalies to velocity at each grid of the model could be calculated conveniently. Therefore, a simultaneous or sequential inversion system of arrival time and gravity data can be built with this gravity modeling approach, which may promote the application of joint inversion of arrival time and gravity data, and provide more reliable structures of the Earth.
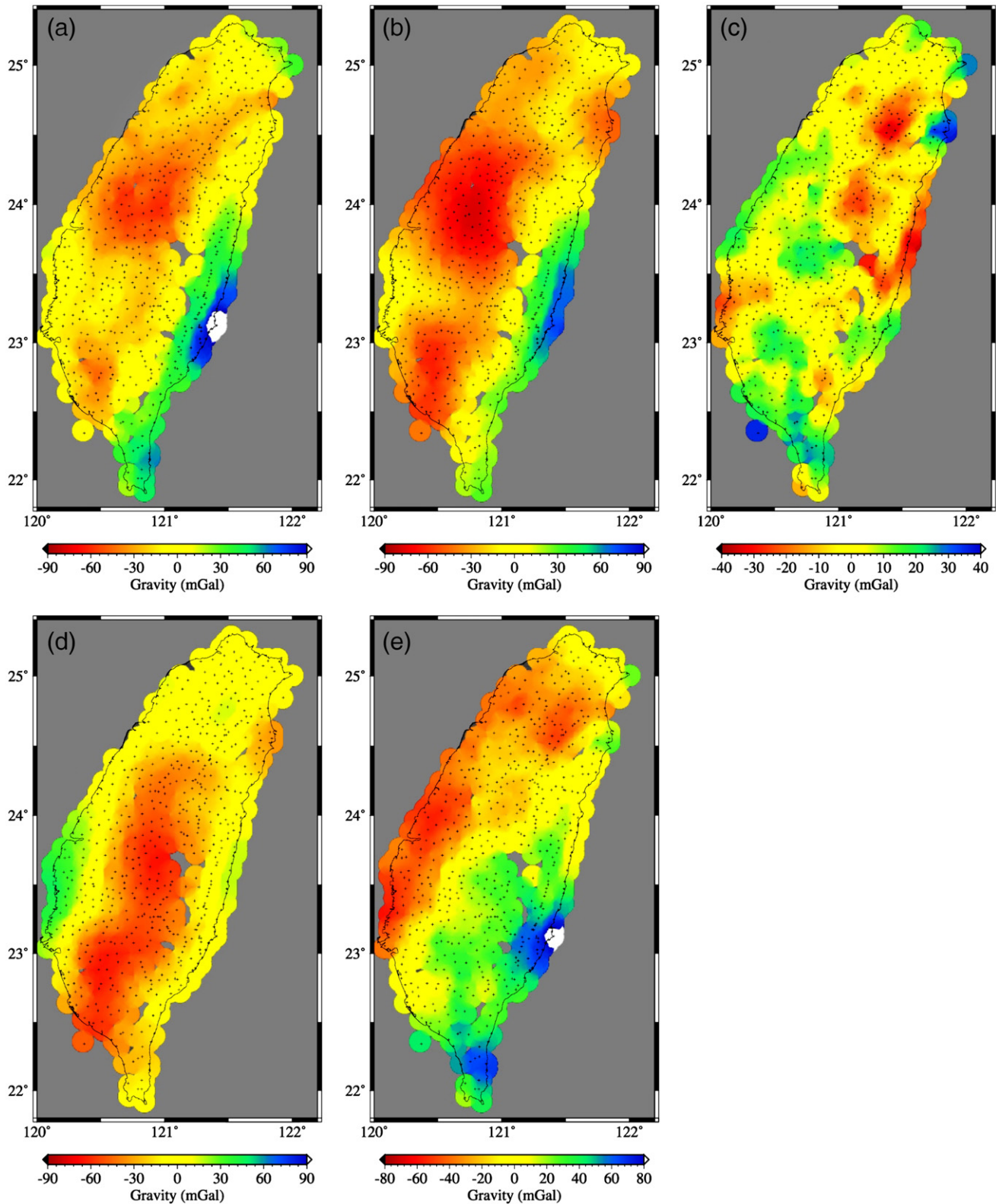
Fig. 8. (a) Bouguer gravity in the Taiwan region. (b) Calculated gravity anomalies from a 3-D velocity model from the joint inversion of arrival time and gravity data. (c) Residuals between Bouguer and calculated gravity shown in figure b. (d) Calculated gravity from 3-D velocity models from inversion of arrival time data only. (e) Residuals between Bouguer and calculated gravity shown in figure d. Small crosses indicate the gravity observation locations.

Moreover, as potential applications, this approach could be used for modeling theoretical gravity fields of the Earth and other spherical planets measured by satellite (Asgharzadeh et al., 2007). Terrain corrections for regional gravity surveys could also be conducted with this approach (Nowell, 1999; Fullea et al., 2008).

40620140435, and 40674046) and the National Basic Research Program of China (2007CB411701).

Appendix A

In the gravity modeling approach, several variables are used to control the required accuracy and efficiency during subdividing prisms into smaller ones: *NS*, *MinPrismS* and *NodeGLQ*. *NS* is the ratio of the minimum distance between the source prism and the observation point vs the maximum side length of the source prism. *MinPrismS* is the lower limit of the minimum side length of the prism. *NodeGLQ* is the number of nodes for GLQ integration, which controls the node spacing of GLQ integration. When the prism is small enough for required accuracy, *NodeGLQ* can be set to be 2 to prevent redundant computations as the integration solution remains essentially unchanged for more nodes. Note that the minimum distance between the prism and the observation point is calculated roughly in spheres ("roughly" because the model parameterization is latitude/longitude/depth based) (Smith et al., 2001). In practice, the approximate distance has no significant influence on the modeling accuracy. The pseudo code of the adaptive scheme for modeling one prism's gravity effects is given below:

Void OnePrismGravityEffect (Gravity, Prism_Information) {
    Calculate DIS and PrismS;
    // **DIS is the minimum distance between the source prism and the observation point.**
    // **PrismS is the maximum side length of the source prism.**
    NS = DIS/PrismS;
    If (DIS>(NS*PrismS) or PrismS<MinPrismS){ // **if the prism is small enough.**
        Collect gravity effect g by GLQ integration;
        Gravity += g;

    }

    else { // **if the prism is still too large**
        zn = 1; xn = 1; yn = 1;
        // **PrismS_rad, PrismS_lon, and PrismS_colat are the side lengths of the prism along**
        // **radius, colatitude, and longitude.**
        Calculate PrismS_rad, PrismS_lon, PrismS_colat;
        if (Dis<(NS* Prism_rad) and PrismS_rad>MinPrismS) zn =2;
        if (Dis<(NS* PrismS_lon) and PrismS_lon>MinPrismS) xn =2;
        if (Dis<(NS* PrismS_colat) and PrismS_cola>MinPrismS t) yn =2;
        for (each new prism){ // recursively call the subroutine for each new prism;
OnePrismGravityEffect (Gravity, new_prism_Information,);

        }

    }

}

The recursive calls of subroutine *OnePrismGravityEffect* are used to subdivide spherical prisms into smaller ones and collect gravity effects of all small prisms.

References

Afnimar, Koketsu, K., Nakagawa, K., 2002. Joint inversion of refraction and gravity data for three-dimensional topography of a sediment–basement interface. Geophys. J. Int. 151, 243–254.

Asgharzadeh, M.F., von Frese, R.R.B., Kim, H.R., Leftwich, T.E., Kim, J.W., 2007. Spherical prism gravity effects by Gauss–Legendre quadrature. Geophys. J. Int. 169, 1–11.

Birch, F., 1961. The velocity of compressional waves in rocks to 10 kilobars, part 2. J. Geophys. Res. 66, 2199–2224.

Bosch, M., Meza, R., Jimenez, R., Honig, A., 2006. Joint gravity and magnetic inversion in 3D using Monte Carlo methods. Geophysics 71, 153–156.

Chen, W.P., Ozalaybey, S., 1998. Correlation between seismic anisotropy and Bouguer gravity anomalies in Tibet and its implications for lithospheric structures. Geophys. J. Int. 135, 93–101.

Christensen, N.I., Mooney, W.D., 1995. Seismic velocity structure and composition of the continental crust: a global view. J. Geophys. Res. 100, 9761–9788.

Fullea, J., Fernandez, M., Zeyen, H., 2008. FA2BOUG — a Fortran 90 code to compute Bouguer gravity anomalies from gridded free-air anomalies: application to the Atlantic – Mediterranean transition zone. Comput. Geosci. 34, 1665–1681.

Gardner, G.H.F., Gardner, L.W., Gregory, A.R., 1974. Formation velocity and density: the diagnostic basics for stratigraphic traps. Geophysics 39, 770–780.

Hao, T.Y., Xu, Y., Suh, M., Xu, Y., Liu, J.H., Zhang, L.L., Dai, M.G., 2007. East Marginal Fault of the Yellow Sea: a part of the Conjunction zone between Sino-Korea and Yangtze Block? In: Zhai, M.-G., Windley, B.F., Kusky, T.M., Meng, Q.R. (Eds.), Geological Society, Special Publication, 280, pp. 281–292.

Ku, C.C., 1977. A direct computation of gravity and magnetic anomalies caused by 2- and 3-dimensional bodies of arbitrary shape and arbitrary magnetic polarization by equivalent point method and a simplified cubic spline. Geophysics 42, 610–622.

Lees, J.M., VanDecar, J.C., 1991. Seismic tomography constrained by Bouguer gravity anomalies: applications in western Washington. Pure Appl. Geophys. 135 (1), 31–52.

Li, Z.W., Roecker, S., Li, Z., Wei, B., Tao, H., Schelochkov, G., Bragin, V., 2009a. Tomographic image of the crust and upper mantle beneath the western Tien Shan from the MANAS broadband deployment: possible evidence for lithospheric delamination. Tectonophysics 477, 49–57.

Li, Z.W., Xu, Y., Hao, T.Y., Xu, Y., 2009b. Vp and Vp/Vs structures in the crust and upper mantle of the Taiwan region, China. Sci China D Earth Sci 52 (7), 975–983.

Masson, F., Achauer, U., Wittlinger, G., 1998. Joint analysis of P-traveltimes teleseismic tomography and gravity modeling for northern Tibet. J. Geodynamics 26 (1), 85–109.

Nielsen, L., Jacobsen, B.H., 2000. Integrated gravity and wide-angle seismic inversion for two-dimensional crustal modeling. Geophys. J. Int. 140, 222–232.

Nowell, D.A.G., 1999. Gravity terrain corrections — an overview. J. Appl. Geophys. 42, 117–134.

Roecker, S., Thurber, C., McPhee, D., 2004. Joint inversion of gravity and arrival time data from Parkfield: new constraints on structure and hypocenter locations near the SAFOD drill site. Geophys. Res. Lett. 31, L12S04 doi: 10.1029/2003GL019396.

Smith, D.A., Robertson, D.S., Milbert, D.G., 2001. Gravitational attraction of local crustal masses in spherical coordinates. J. Geod. 74, 783–795.

Stroud, A.H., Secrest, D., 1966. Gaussian Quadrature Formulas. Prentice-Hall, New Jersey.

Vermeesch, P.M., Morgan, J.V., Christeson, G.L., Barton, P.J., Surendra, A., 2009. Three-dimensional joint inversion of traveltime and gravity across the Chicxulub impact crater. J. Geophys. Res. 114, B02105 doi: 10.1029/2008JB005776.

von Frese, R.R.B., Hinz, W.J., Braile, L.W., 1981a. Spherical earth gravity and magnetic anomaly analysis by equivalent point source inversion. Earth Planet Sci. Lett. 53, 69–83.

Von Frese, R.R.B., Hinze, W.J., Braile, L.W., Luca, A.J., 1981b. Spherical earth gravity and magnetic anomaly modeling by Gauss–Legendre quadrature integration. J. Geophys. 49, 234–242.

von Frese, R.R.B., Jones, M.B., Kim, J.W., Li, W.S., 1997. Spectral correlation of magnetic and gravity anomalies of Ohio. Geophysics 62, 365–380.

von Frese, R.R.B., Tan, L., Kim, J.W., Bentley, C.R., 1999. Antarctic crustal modeling from the spectral correlation of free-air gravity anomalies with the terrain. J. Geophys. Res. 104, 25275–25296.

Xu, Y., Hao, T., Li, Z., Duan, Q., Zhang, L., 2009. Regional gravity anomaly separation using wavelet transform and spectrum analysis. J. Geophys. Eng. 6, 279–287.

Yen, H.Y., Yeh, Y.H., Lin, C.H., Chen, K.J., Tsai, Y.B., 1995. Gravity survey of Taiwan. J. Phys. Earth 43, 685–696.